Available online at www.sciencedirect.com
SCIENCE DIRECT®
International Journal of Heat and Mass Transfer 47 (2004) 4673–4684
International Journal of HEAT and MASS TRANSFER
www.elsevier.com/locate/ijhmt

Numerical study of the effects of rotation on heat transfer in channels with and without ribs

Joon Sang Lee [a], Ning Meng [b], Richard H. Pletcher [a,*], Yang Liu [c]

[a] Department of Mechanical Engineering, 2025 Black Engr. Building, Iowa State University, Ames, IA 50011, United States
[b] VasSol Inc., Chicago, IL 60607, United States
[c] Department of Mechanical Engineering, 187A Rhodes Hall, Cornell University, Ithaca, NY 14853, United States

Received 26 August 2003; received in revised form 2 June 2004

Abstract

Large eddy simulation of rotating channel and ribbed channel flows with and without heat transfer is reported. The rotation axis is parallel to the spanwise direction of the parallel plate channel. An implicit finite-volume scheme was used to solve the preconditioned time-dependent filtered Navier–Stokes equations using a dynamic subgrid-scale model to account for the subgrid-scale effects. The distribution of mean velocity and mean temperature were influenced by system rotation, transforming from a symmetric profile into a non-symmetric profile. The shift of peak values was toward the stable side of the channel.

Near the stable (leading) side, the turbulent intensities and heat transfer were suppressed, but turbulence was enhanced with increasing shear stress and turbulent kinetic energy near the unstable (trailing) side.

Keywords: Large eddy simulation; Finite volume formulation; Compressible Navier–Stokes equations; Rotation; Ribbed channel

1. Introduction

Turbulent rotating flows are of considerable interest in a variety of industrial, geophysical and astrophysical applications. Examples are natural flows like ocean currents, estuaries and atmospheric boundary layers, and engineering flows in rotating devices such as turbines, pumps, compressors and cyclone separators. It is well known that system rotation affects both the mean motion and the turbulence statistics. Many rotational-induced flow phenomena have been reviewed by Tritton [1] and Hopfinger [2].

System rotation influences turbulence in several ways: for example, it may decrease energy transfer from large to small scales or reduce turbulence dissipation and the decay rate of turbulence energy. In rotating channel flow, system rotation can both stabilize and destabilize the flow. On the unstable side, Coriolis forces enhance turbulence production and increase the intensity of turbulence, while on the stable side, Coriolis forces reduce turbulence production and decrease the intensity of turbulence (Piomelli [3]).

Most large eddy simulations (LES) of flows with heat transfer reported to date employed an incompressible formulation and treated temperature as a passive scalar. However, compressible formulations have been employed in a few recent works (Moin et al. [4] and Dailey et al. [5]) where the coupling between velocity and temperature fields were considered.

Rotating channel flows have been investigated experimentally (Johnston [6]; Han et al. [7]) and numerically (Piomelli [3]; Kristofferson and Anderson [8]). However, very little information is available for rotating channel flow with heat transfer, especially from the LES or DNS community.

The flow over two and/or three-dimensional obstacles of different shapes and sizes with and without

* Corresponding author. Tel.: +1-515-294-2656; fax: +1-515-294-3261.
E-mail address: pletcher@iastate.edu (R.H. Pletcher).

0017-9310/$ - see front matter © 2004 Elsevier Ltd. All rights reserved.
doi:10.1016/j.ijheatmasstransfer.2004.06.006

Nomenclature

C_d, C_I	dynamic subgrid-scale model coefficients
G	filter function
Gr	Grashof number
h	heat transfer coefficient, or specific enthalpy
L_{ref}	reference length
Ma	Mach number
m	pseudo-time index
Nu	Nusselt number $(= 2h(r_2 - r_1)/k_b)$
n	physical time index
ni, nj, nk	control volume number in streamwise, radius and circumferential directions
$\vec{n}$	unit normal vector
p_p	periodic component of the pressure
Pr	Prandtl number $(= \mu c_p/k)$
Pr_t	turbulent Prandtl number
q_j	heat flux vector
R	gas constant
Re	generic Reynolds number
S_{ij}	strain rate tensor
T	thermodynamic temperature
T_b	bulk temperature
T_{ij}	test filtered stress tensor
t	physical time
$[U]$	vector of conserved variables
u_τ	friction velocity $(= \sqrt{\tau_w/\rho_w})$
u, v, w	Cartesian velocity components in x, y, z directions
x, y, z	Cartesian coordinates

Greek symbols

γ	ratio of specific heats
Δ	grid filter width
$\hat{\Delta}$	test filter width
δ	Kronecker delta
μ	molecular dynamic viscosity
μ_t	subgrid-scale turbulent viscosity
ν	molecular kinematic viscosity $(= \mu/\rho)$
ν_t	subgrid-scale turbulent kinematic viscosity
ρ	thermodynamic density
σ_{ij}	shear stress tensor
τ_{ij}	subgrid-scale stress tensor
Ω	cell volume

Subscripts

b	bulk property
i, j, k	indices for Cartesian coordinates
p	periodic component
rms	root-mean-square
w	wall value
x, y, z	associated with Cartesian direction

Superscripts and other symbols

$'$	fluctuation with respect to ensemble average, or unresolved or subgrid-scale component of filtered quantity
$\overline{\ }$	resolved or large scale component of filtered quantity
$\tilde{\ }$	resolved or large scale component of Favre filtered quantity
$\hat{\ }$	nonlinear function of Favre filtered quantity
$< >$	ensemble averaged quantity

rotation have been studied extensively by numerous investigators due to its importance to engineering applications. Among these are flows in turbines, pumps, diffusers, and electronic components (Matsubara and Alfreson [9]). In many of these applications, enhanced surfaces and rotation significantly alter the structure of the turbulence. Han et al. [10] conducted an experimental study to investigate the effect of rib geometry on friction factor and Stanton number for turbulent flow. It was found that the shape of the rib affected the friction factor, while a modest effect was observed on the heat transfer.

Bergeles and Athanassiadis [11] studied the influence of the streamwise length of a rib on reattachment length and showed that a sudden decrease in reattachment length from 11 to 3 rib heights was observed when the length to height ratio of a rib was greater than 4. Sparrow and Tao [12] used the naphthalene sublimation technique in flat rectangular channels of large aspect ratios with obstacles situated on one of the walls of the channel and oriented transversely to the flow direction. The results showed a substantial enhancement of Sherwood numbers (Sh) compared with the smooth-wall duct. Drain and Martin [13] performed laser Doppler velocimetry (LDV) measurements of the fully developed water flow in a rectangular duct with one surface roughened with a periodic array of elements. They found that the k–ϵ turbulence model tended to seriously underestimate the reattachment length, which is an important indicator of turbulence structure.

According to Wagner et al. [14], approximately 75% of the estimated uncertainty in calculating the heat transfer coefficient was due to the temperature measurement error. Furthermore, it can be very difficult and expensive to obtain detailed information about the flow distribution in a ribbed rotating passage experimentally. Large eddy simulation presents an attractive alternative to experiments for studying details of such flows. The

goal of the present study was to perform a large eddy simulation of rotating turbulent flow in a plane channel with and without transverse square ribs on the walls. Periodic and step periodic (Dailey et al. [5]) boundary conditions were used at the inflow and outflow boundaries since fully developed channel flows were considered. This assumption allows the computed domain to be limited to the region between two adjacent ribs so that a reasonable computational grid can be used.

2. Governing equations

The governing equations for large eddy simulation were obtained by filtering the unsteady three-dimensional compressible Navier–Stokes equations. The filter, which separates the effects of the large-scale and small-scale motions, can be written in terms of a convolution integral as

$$\bar{f}(\vec{x},t)=\int_D G(\vec{x}-\vec{\xi})f(\vec{\xi},t)\,\mathrm{d}\vec{\xi} \tag{1}$$

where G is some spatial filter with a width on the order of the grid spacing, and D is the flow domain.

For compressible flows, the Favre-averaged filter is introduced which can be defined by

$$\widetilde{f}=\frac{\overline{\rho f}}{\bar{\rho}}. \tag{2}$$

The resulting equations were non-dimensionalized with respect to a reference length δ, velocity V_r, density ρ_r, and viscosity μ_r. For the simulations in this paper, δ is the half height of the channel, and V_r is the bulk velocity at the inlet. The resulting Favre-filtered non-dimensional compressible forms of equations for conservation of mass, momentum are given as below:

$$\frac{\partial\bar{\rho}}{\partial t}+\frac{\partial(\bar{\rho}\tilde{u}_i)}{\partial x_i}=0 \tag{3}$$

$$\frac{\partial(\bar{\rho}\tilde{u}_i)}{\partial t}+\frac{\partial(\bar{\rho}\tilde{u}_i\tilde{u}_j)}{\partial x_j}=-\frac{\partial\bar{p}}{\partial x_i}+\frac{\partial\widetilde{\sigma}_{ij}}{\partial x_j}-\frac{\partial\tau_{ij}}{\partial x_j}+2\epsilon_{ij3}\Omega\widetilde{u}_j \tag{4}$$

Vreman et al. [15] derived a conservative form of the energy equation as below,

$$\begin{aligned}\frac{\partial(\bar{\rho}\tilde{E})}{\partial t}+\frac{\partial[(\bar{\rho}\tilde{E}+\bar{p})\tilde{u}_j]}{\partial x_j}\\ =-\frac{\partial(\tilde{u}_i\tilde{\sigma}_{ij})}{\partial x_j}-\frac{\partial\tilde{q}_j}{\partial x_j}-\frac{\partial q_{tj}}{\partial x_j}-\alpha-\pi-\epsilon\end{aligned} \tag{5}$$

In the equations above, $2\epsilon_{ij3}\Omega\widetilde{u}_j$ represents the Coriolis force, ϵ_{ij3} is Levi–Civita's alternating tensor and Ω is the angular velocity of the system. The resolved total energy is $\tilde{E}=C_\mathrm{v}\tilde{T}+\frac{1}{2}\tilde{u}_i\tilde{u}_i$, the viscous stress tensor is

$$\widetilde{\sigma}_{ij}=\frac{2\mu}{Re_\mathrm{L}}(\widetilde{S}_{ij}) \tag{6}$$

and the strain rate tensor and heat flux vectors are

$$\widetilde{S}_{ij}=\frac{1}{2}\left(\frac{\partial\tilde{u}_i}{\partial x_j}+\frac{\partial\tilde{u}_j}{\partial x_i}\right) \tag{7}$$

$$\tilde{q}_j=-\frac{c_p}{Re_\mathrm{L}}\frac{\mu}{Pr}\frac{\partial\tilde{T}}{\partial x_j} \tag{8}$$

and the Favre filtered equation of state is $\bar{p}=\bar{\rho}R\widetilde{T}$. The viscosity μ and thermal conductivity k were evaluated by using the power law.

$$\frac{\mu}{\mu_0}=\left(\frac{T}{T_0}\right)^{0.7},\quad \frac{k}{k_0}=\left(\frac{T}{T_0}\right)^{0.7} \tag{9}$$

The effects of the small scales are present in the above equations through the SGS stress tensor in the filtered momentum equation

$$\tau_{ij}=\bar{\rho}(\widetilde{u_iu_j}-\tilde{u}_i\tilde{u}_j). \tag{10}$$

and the SGS heat flux and other quantities in the filtered energy equation,

$$q_{tj}=\bar{\rho}c_\mathrm{v}(\widetilde{Tu_j}-\tilde{T}\tilde{u}_j), \tag{11}$$

$$\alpha=\tilde{u}_i\frac{\partial(\bar{\rho}\tau_{ij})}{\partial x_j}, \tag{12}$$

$$\pi=\overline{p\frac{\partial u_i}{x_i}}-\bar{p}\frac{\partial\tilde{u}_i}{\partial x_i}, \tag{13}$$

$$\epsilon=\overline{\sigma_{ij}\frac{\partial u_j}{x_i}}-\widetilde{\sigma_{ij}}\frac{\partial\tilde{u}_i}{\partial x_j}. \tag{14}$$

For this research, the first three terms on the right hand side of the energy equation were computed, but the remaining three terms (α,π,ϵ) were neglected due to their relative smaller magnitudes.

3. Numerical method

In the present research, a compressible LES formulation was used, which also permitted the subgrid-scale turbulent Prandtl number to be computed dynamically. A finite volume method was used to numerically solve the governing equations. The code used Cartesian hexahedral control volumes, and solved for the primitive variables (p,u,v,w,T) that were stored at the cell centers. Besides the physical time integration, pseudo time iterations were performed to resolve nonlinearities in the algebraic formulation and to implement the low Mach number preconditioning using an implicit LU-SGS scheme. The low Mach number preconditioning was used to enable the compressible code to work efficiently

at nearly incompressible speeds. The solver is second-order accurate in both space and time (Dailey and Pletcher [16]). The multiblock code was parallelized using the message passing interface (MPI). The computations were carried out on an IBM SP2 (Minnesota Supercomputing Institute) using 17 processors.

When property variations are taken into account, flows with heating or cooling do not attain a fully-developed state. However, experiments show that far downstream of the entry region, a slowly evolving quasi-developed state exists. Dailey [16] showed that a short section of the downstream region could be computed in a "stepwise periodic" manner with the following streamwise boundary conditions.

$$\begin{aligned} \rho u(0,y) &= \rho u(L_x,y) \\ v(0,y) &= v(L_x,y) \\ w(0,y) &= w(L_x,y) \\ p_p(0,y) &= p_p(L_x,y) \\ T(0,y) &= T(L_x,y) - \Delta T_x \end{aligned} \tag{15}$$

where L_x is the length of the computation domain in the streamwise direction and $\bar{p}_p$ is the periodic component of the pressure $\bar{p}(x,y,z,t) = \beta x + \bar{p}_p(x,y,z,t)$, where β is the average streamwise pressure gradient. The temperature difference ΔT_x is computed from an energy balance utilizing the uniform heat flux imposed and the mass flux. All primitive variables $(\tilde{p}, \tilde{u}_i, \tilde{T})$ were assumed to be periodic in the spanwise (z) direction.

The conventional Reynolds (or ensemble) average of a quantity is denoted as $\langle\ \rangle$, and the Favre ensemble average as $\{\ \}$, where

$$\{f\} = \langle \rho f \rangle / \langle \rho \rangle. \tag{16}$$

A single prime ($'$), and a double prime ($''$), denote the turbulent fluctuations with respect to the Reynolds or Favre ensemble average, respectively.

The velocity fluctuations were obtained at each time step as

$$\tilde{u}_i'(x,y) = \tilde{u}_i(x,y) - \langle \tilde{u}_i \rangle_z(x,y) \tag{17}$$

where $\langle\ \rangle_z$ denotes an average in the z direction only. The ensemble averaged root-mean-square (rms) values were subsequently obtained as

$$\tilde{u}_{\mathrm{rms}}(x,y) = \sqrt{\frac{< \tilde{u}'(x,y)^2 >}{N_{\mathrm{stat}}}} \tag{18}$$

where $< >$ denotes an average in z and in time, and N_{stat} is the number of time steps used to compute the statistics. The rotating channel flow simulation began with a fully-developed channel flow solution obtained from previous research, and needed about 10,000 physical time steps to become statistically stationary under the influence of the system rotation. The turbulent statistics (e.g. $\tilde{u}_{\mathrm{rms}}$) were collected over the following 10,000 physical time steps.

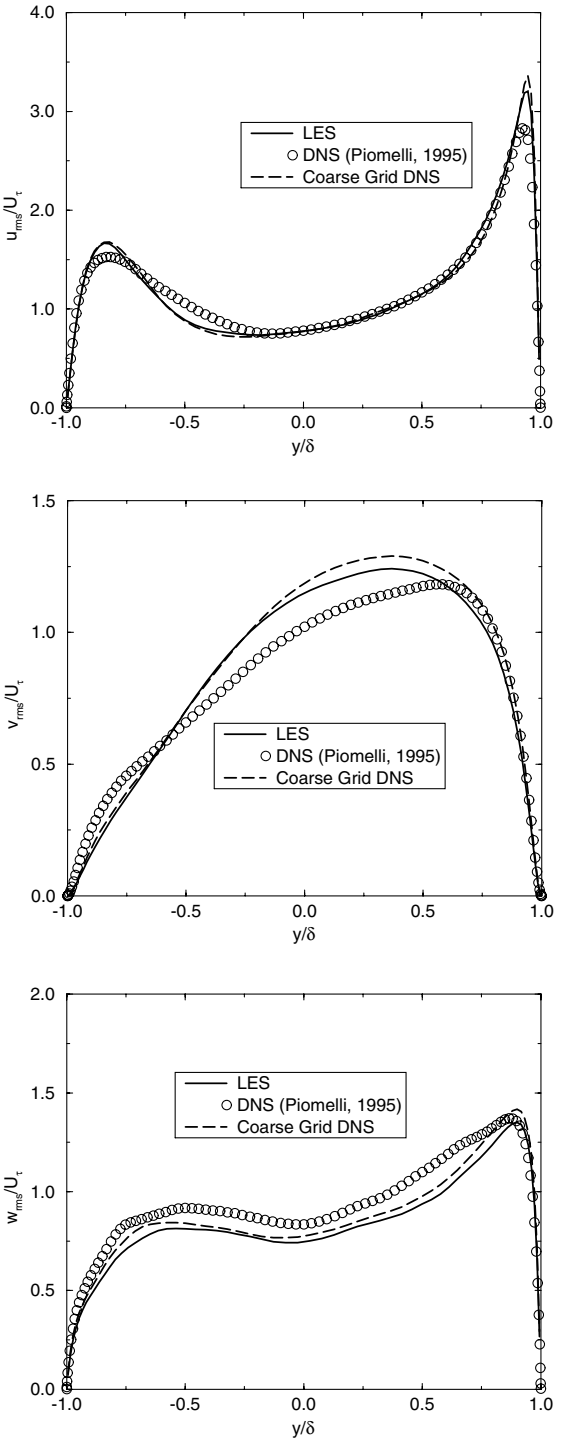

Fig. 1. Streamwise, normal, and spanwise velocity rms distributions, isothermal case.

Shear stress and heat flux distributions were also computed as part of the turbulence statistics. The computed shear stress contributions were

$$\tau_{\text{res}} = - < \rho \tilde{u}'' \tilde{v}'' > \tag{19}$$

$$\tau_{\text{vis}} = - < \frac{\mu}{Re} \frac{\partial \tilde{u}}{\partial y} > \tag{20}$$

$$\tau_{\text{sgs}} = - < \mu_{\text{t}} \frac{\partial \tilde{u}}{\partial y} > \tag{21}$$

where τ_{res} is the resolvable Reynolds shear stress, τ_{vis} is the viscous shear stress, and τ_{sgs} is the modeled SGS stress. Similarly, the computed heat flux contributions were

$$q_{\text{res}} = - < \rho \tilde{v}'' \widetilde{T}'' > \tag{22}$$

$$q_{\text{con}} = - < \frac{\mu c_p}{Re\,Pr} \frac{\partial \widetilde{T}}{\partial y} > \tag{23}$$

$$q_{\text{sgs}} = - < \frac{\mu_{\text{t}} c_{\text{v}}}{Pr_{\text{t}}} \frac{\partial \widetilde{T}}{\partial y} > \tag{24}$$

where q_{res} is the resolvable turbulent heat flux, q_{con} is the heat conduction, and q_{sgs} is the modeled SGS heat flux.

4. Dynamic subgrid scale stress model

Dynamic modeling of the subgrid-scale stresses was introduced by Germano et al. [17]. Unlike the Smagorinsky model, the model coefficients, C_{d}, and C_{I}, are computed dynamically as the computation progresses. Before the dynamic model coefficients are introduced, a test filter should be given by

$$\hat{f}(x) = \int_D f(x') \widehat{G}(x, x')\, \mathrm{d}x' \tag{25}$$

where $\widehat{G}$ is the test filter. In this work, the test filter was two times larger than the filter function G. The dynamic model for this research was based on Wang's [18] derivation. By use of Lilly's [19] approach, the unknown parameters, C_{d}, and C_{I} can be determined as

$$C_{\text{d}} = \frac{-1}{2\Delta^2} \frac{< D_{ij} P_{ij} >}{< P_{ij} P_{ij} >} \tag{26}$$

$$C_{\text{I}} = \frac{1}{\Delta^2} \frac{< \overline{\rho} \widehat{\widetilde{u}_k \widetilde{u}_k} - (\widehat{\overline{\rho} \widetilde{u}_k} \widehat{\overline{\rho} \widetilde{u}_k} / \hat{\overline{\rho}}) >}{< 2(\hat{\overline{\rho}} \alpha |\hat{\widetilde{S}}|^2 - \overline{\rho} |\widetilde{S}|^2) >} \tag{27}$$

where $<\ >$ denotes spatial averaging along the streamwise and spanwise directions of the flow, $|S|$ is the magnitude of the strain rate tensor, Δ is the filtered width $(= (\Delta_x \Delta_y \Delta_z))^{1/3}$, and α is the strain grid ratio $(= \hat{\Delta}/\Delta)$. The superscripts $(\hat{\ }, \bar{\ }, \tilde{\ })$ denote the nonlinear function of a Favre filtered quantity, large scale component of filtered quantity, and large scale component of Favre filtered quantity, respectively. D_{ij} and P_{ij} are defined as

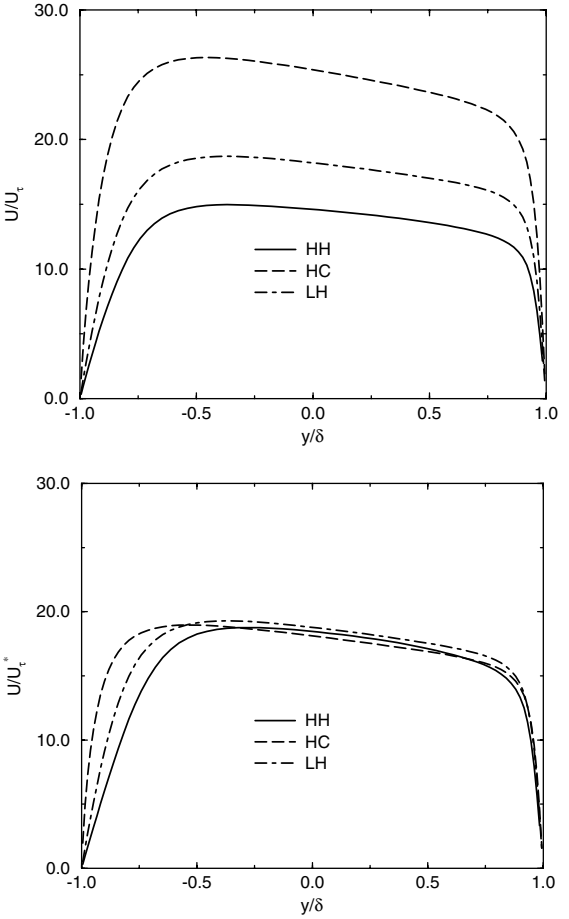

Fig. 2. Profiles of U velocity in global and semi-local coordinates.

Table 1
Summary of the numerical calculations

Case	$u_{\tau,\text{top}}$	$u_{\tau,\text{bot}}$	$\frac{\Delta T}{T_{\text{b}}}$	Nu_{top}	Nu_{bot}	$C_{\text{f,top}}$	$C_{\text{f,bot}}$
Low heating	0.0701	0.0470	−0.0585	60.04	20.70	0.00551	0.00228
High heating	0.0889	0.0759	−0.594	66.29	18.47	0.00587	0.00279
High cooling	0.0686	0.0263	+0.471	62.14	18.57	0.00544	0.00212

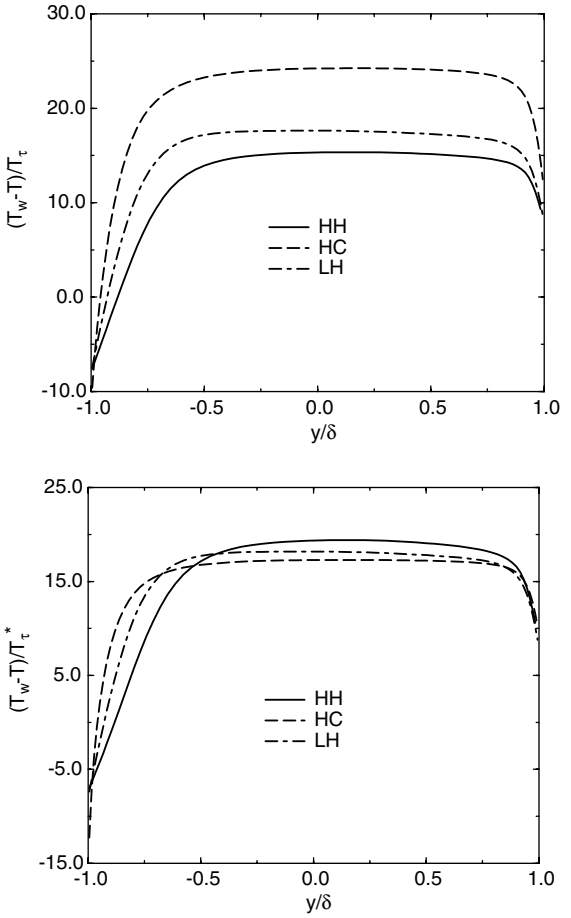

Fig. 3. Profiles of temperature in global and semi-local coordinates; T_w is the average of the two wall temperatures.

$$D_{ij} = \frac{\overline{\rho}\widetilde{\widehat{u_i}\widehat{u_j}} - \widehat{\overline{\rho}\widetilde{u_i}}\widehat{\overline{\rho}\widetilde{u_j}}}{\widehat{\overline{\rho}}} - \frac{1}{3}(T_{kk} - \widehat{\tau_{kk}})\delta_{ij} \tag{28}$$

$$P_{ij} = \hat{\overline{\rho}}|\hat{\widetilde{S}}|\left(\widehat{\widetilde{S}_{ij}} - \frac{1}{3}\widehat{\widetilde{S}_{kk}}\delta_{ij}\right) - \left[\overline{\rho}|\widetilde{S}|\left(\widetilde{S}_{ij} - \frac{1}{3}\widetilde{S}_{kk}\delta_{ij}\right)\right] \tag{29}$$

Many researchers neglect the isotropic part of SGS stress tensor on the grounds that it is not only negligible compared to the thermodynamic pressure, but also the calculation is unstable if the isotropic part of the SGS stress tensor is not neglected (Moin et al. [4]; Vreman et al. [15]) Therefore, C_I was set to zero in this study.

The turbulent heat flux in the energy equation needs to be modeled following Wang [18].

$$q_{tj} = -\overline{\rho}v_H\frac{\partial\widetilde{T}}{\partial x_j} \tag{30}$$

where the SGS eddy heat diffusivity is

$$v_H = -\frac{C_d\overline{\Delta}^2}{Pr_t}|\widetilde{S}_{ij}| \tag{31}$$

and the turbulent Prandtl number (Pr_t) is

$$Pr_t = -C_d\overline{\Delta}^2\frac{< F_kF_k >}{< E_kF_k >} \tag{32}$$

E_k and F_k are defined as

$$E_k = \frac{1}{\hat{\overline{\rho}}}\widehat{\overline{\rho}\widetilde{u_k}}\widehat{\overline{\rho}\widetilde{T}} - \hat{\rho}\widehat{\widetilde{u_k}\widetilde{T}} \tag{33}$$

$$F_k = \hat{\overline{\Delta}}^2\hat{\overline{\rho}}|\hat{\widetilde{S}}|\frac{\partial\hat{\widetilde{T}}}{\partial x_k} - \overline{\Delta}^2\overline{\rho}|\widetilde{S}|\frac{\partial\widehat{\widetilde{T}}}{\partial x_k} \tag{34}$$

5. Results and discussion

5.1. Channel flows without ribs

The simulations were run with a domain size of $2\pi\times2\times\pi$ with a grid that had $48\times64\times48$ control volumes in the x, y and z directions, respectively. A grid study (Dailey [5]) has shown that for low heating simulations without rotation, this grid size provided accurate results compared to DNS and experimental data. The near wall region is well-resolved. For the high heating case, the y^+ (based on averaged friction velocity) at the first grid point near the wall is less than 0.5.

No-slip velocity and zero normal pressure gradient boundary conditions were enforced at the upper and lower walls. The isoflux thermal wall boundary conditions were used for both walls. The dimensionless wall heat flux ($q_w = \frac{q_w''}{C_p\rho_{ref}U_{ref}T_{ref}}$) was kept at 2×10^{-4} for the low heating case, and kept at 2×10^{-3} and -2×10^{-3} for high heating and high cooling cases, respectively.

Calculations were performed for four different cases: no heat transfer, low heating, high heating, and high cooling. The Reynolds number $Re = U(2\delta)/v$ (based on the channel width, 2δ, and reference velocity, U) was 5600, and the rotation number $Ro_b = |\Omega|(2\delta)/U$ was 0.144. (Note that Rossby number is defined as $Ro = U/(2|\Omega|D_H)$, which is a quarter of the inverse of the rotation number Ro_b.)

The results from the first case were compared with the DNS results (grid $96\times97\times128$) of Piomelli [3] for the isothermal rotating channel flow with $Re_b = U_b(2\delta)/v = 5700$ and $Ro_b = 0.144$. Since it was found from previous LES simulations that the contribution of SGS model to turbulent flux is small, it is interesting to do a simulation (coarse grid DNS) without any model using the same grid resolution as that of LES ($48\times64\times48$).

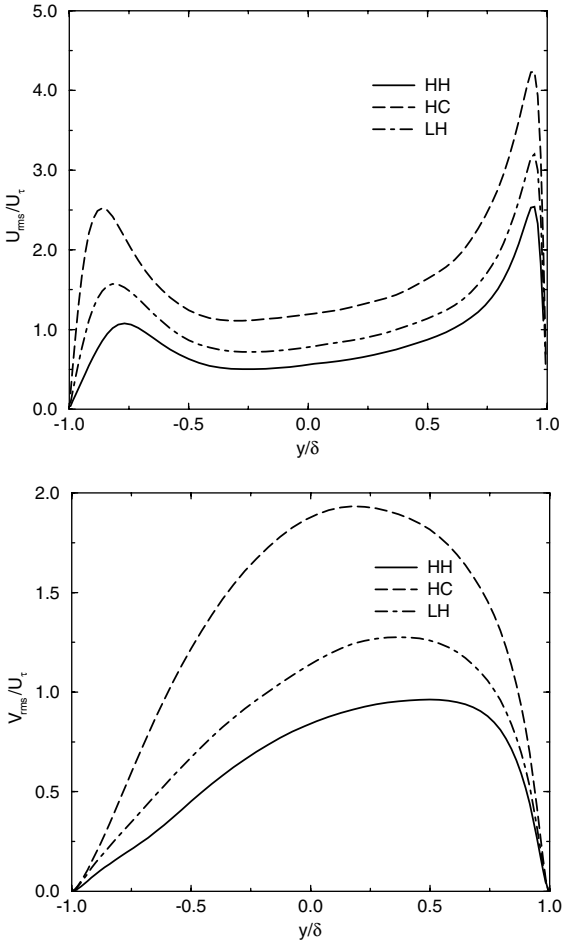

Fig. 4. Velocity rms in x and y.

Fig. 1 shows the rms distributions (normalized by the average value of u_τ on two walls) for velocity fluctuations in x, y, and z directions, respectively. The rms fluctuations are enhanced near the unstable side (trailing, $y = 1.0$) but reduced near the stable side of the channel (leading, $y = -1.0$). It is noticeable that the profile of v_{rms} becomes a one-peak distribution instead of the two-peak distribution obtained without rotation. This is also due to the fact that the Coriolis force acts in the y direction. These results agree well with those of Piomelli's [3], validating the current LES formulation. The coarse grid DNS data, in general, slightly overestimate velocity fluctuations compared with the LES data. There is an overshoot for the coarse grid DNS in the prediction of velocity fluctuations near the upper (top) wall. The reason might be that the current grid resolution ($48 \times 64 \times 48$) is not fine enough for DNS. LES has better damping behavior at the near wall region with the aid of the SGS model.

Table 1 lists some parameters at both walls where the friction velocity is

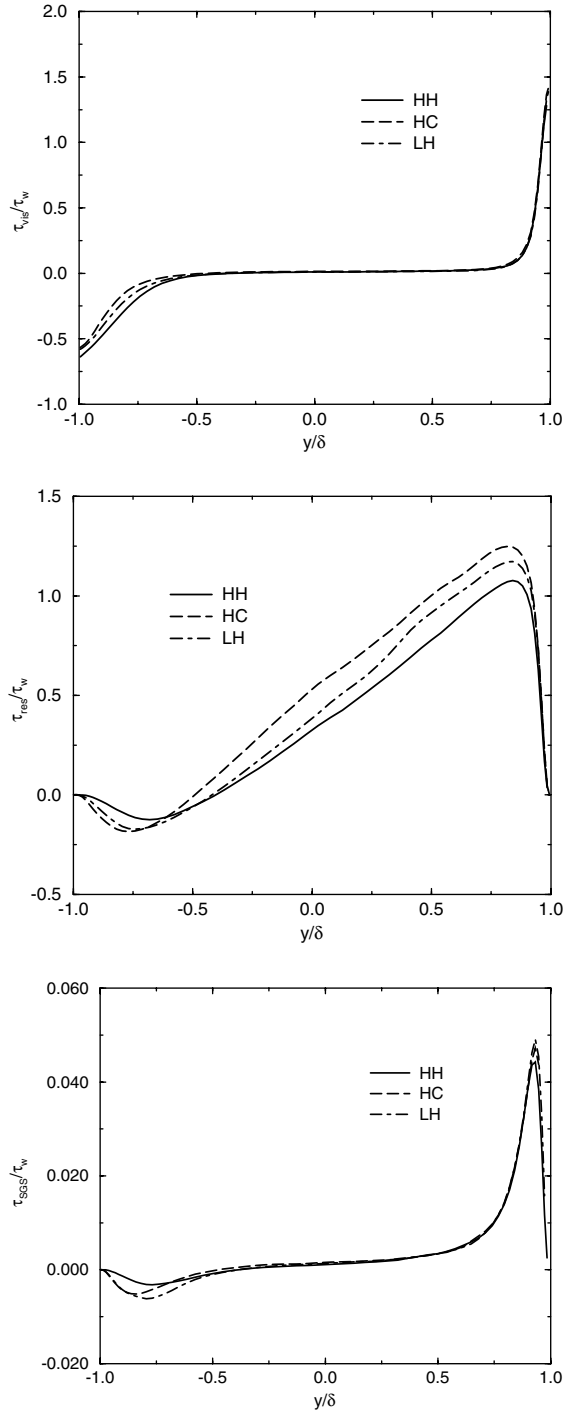

Fig. 5. Viscous, resolved, and SGS stresses.

$$u_\tau = \sqrt{\frac{\tau_w}{\rho_w}} \tag{35}$$

$\Delta T = T_{w,top} - T_{w,bot}$ is the temperature change across the normal direction, and T_b is the bulk temperature.

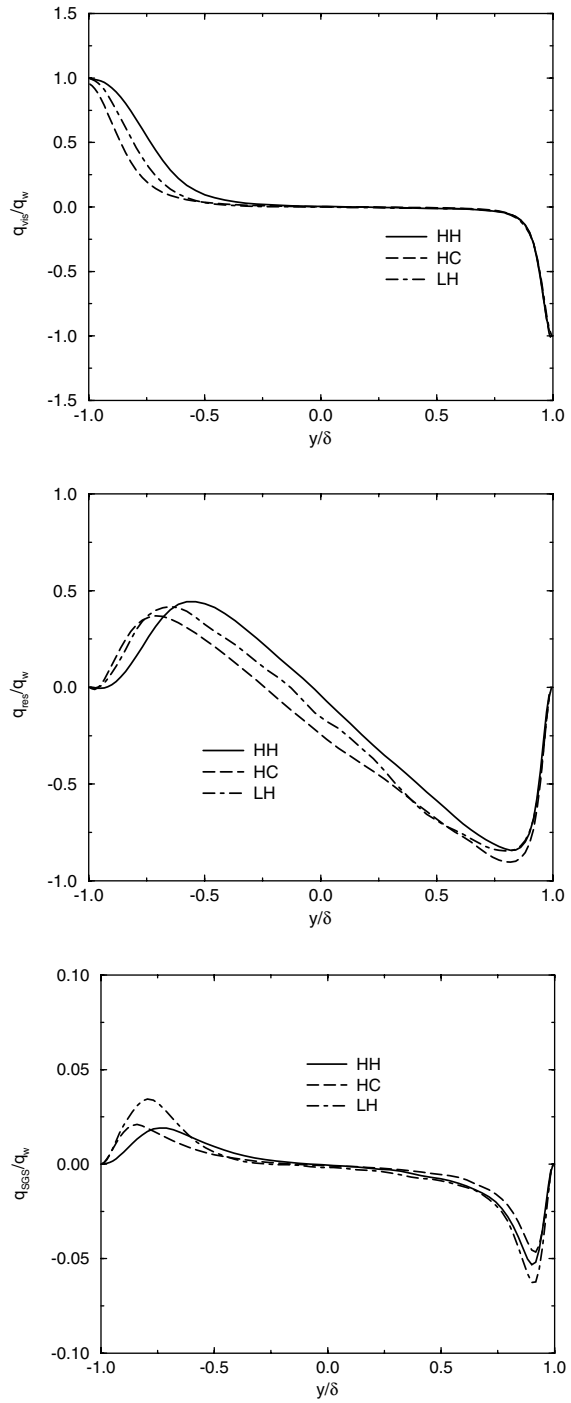

Fig. 6. Viscous, resolved, and SGS heat fluxes.

$$T_b = \frac{\int_{-1}^{1} \rho u T \, dy}{\int_{-1}^{1} \rho u \, dy} \tag{36}$$

The Nusselt numbers and the friction coefficient are defined as

Table 2
Parameters for three rotational cases

Case	Ro_b	q_w
I	0.00 (no rotation)	2×10^{-3}
II	0.15 (medium rotation)	2×10^{-3}
III	0.30 (high rotation)	2×10^{-3}

$$Nu = \frac{2h\delta}{k_b} \tag{37}$$

$$C_f = \frac{\tau_w}{\frac{1}{2}\rho_b U_b^2} \tag{38}$$

where h is the heat transfer coefficient, k_b the bulk thermal conductivity, ρ_b and U_b are the bulk density and velocity, respectively.

The ratio of friction velocity at the top wall to that at the bottom wall is approximately 2.6, 1.5, and 1.2 for high cooling, low heating, and high heating, respectively. The high cooling case reacted most strongly to the system rotation as indicated by the significant difference between its two friction velocities. The low heating case has a relative temperature change ($\Delta T/T_b$) of 5.85%, but the high heating and high cooling case have much larger temperature change, namely, 59.4% and 47.1%, respectively. It is found that Nusselt number at the top wall (or the unstable side) is slightly more than three times as large as that at the bottom wall (or the stable side). Friction coefficients at the top wall are around two times larger than those at the bottom wall.

Fig. 2 illustrates the streamwise velocity profiles for high heating (HH), high cooling (HC) and low heating (LH) cases in global and semi-local coordinate systems. The influence of rotation is reflected in the asymmetric distribution of velocities for all three cases. The U velocity profile for HC is above that of LH, but the profile for HH is below that of LH. This is, in part, because in the figures the streamwise velocity has been normalized by the average of u_τ at the two walls and u_τ is significantly influenced by property variations in the flow.

Huang et al. [20] have proposed a semi-local definition of friction velocity, in which the local density is used instead of the wall density.

$$u_\tau^* = \sqrt{\frac{\tau_w}{\rho}}$$

When u_τ^* is used to replace u_τ, the resulting semi-local distribution shows that the three profiles collapsed toward the low heating curve.

The mean temperature profiles are plotted in global coordinates and semi-local coordinates in Fig. 3. The T_τ and T_τ^* are defined as below,

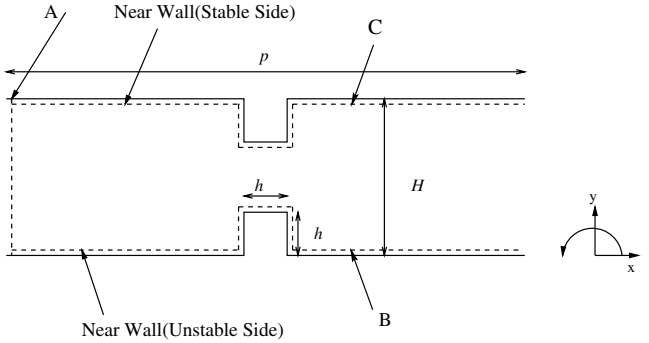

Fig. 7. Schematic of the computational domain for the ribbed channel.

$$T_\tau = \frac{q_w}{\rho_w c_p u_\tau}, \quad T_\tau^* = \frac{q_w}{\rho(y) c_p u_\tau^*} \tag{39}$$

As for the velocity profiles, the high heating and high cooling temperature profiles in global coordinates departed from the low heating results. However, the spread in the curves is greatly decreased when semi-local coordinates are used. Again, non-symmetry has been observed in those averaged temperature distributions.

The root-mean-squares of the velocity fluctuations with respect to Reynolds ensemble averages are plotted in global coordinates in Fig. 4. Again, larger velocity fluctuations were found near the unstable side as a consequence of rotation, and the high heating and cooling values varied significantly from the low heating result. Again, the values are normalized by the average of u_τ for the two walls.

Fig. 5 shows the viscous, resolved, and modeled SGS shear stress distributions normalized by the average of the two wall shear stresses. The results indicate that rotation increased the shear stress near the unstable side but suppressed the shear stress near the stable side.

Fig. 6 shows the heat conduction, resolved turbulent heat flux and modeled SGS heat flux distributions normalized by the wall heat flux. The same trends were observed as for the shear stress distributions, suggesting that heat transfer was increased near the unstable side but decreased near the stable side because of rotation.

5.2. Channel flows with ribs

The geometry and coordinate system for the ribbed channel cases are depicted in Fig. 7. The ribs were directly opposed and aligned normal to the main flow direction. The ratio of rib spacing to rib height was 10 and rib height to channel height was 0.1. Calculations were performed for three different cases with a $(72 \times 62 \times 72)$ grid size: no rotation, medium rotation, and high rotation. Uniform heat flux was applied to the channel to investigate the effects of property variations with temperature. The Reynolds number was 5600. The detailed information is given in Table 2.

Fig. 8 shows the corresponding rms distributions for turbulent intensities in the x, y, and z directions at section A. As we observed earlier, the Coriolis force tends to reduce and enhance the turbulent intensities near the stable side, and unstable side, respectively.

The friction coefficient (C_f) and the Nusselt number (Nu) along the wall at sections B and C are shown in Fig. 9. Since the profile is symmetric, only one distribution of C_f is shown for Case I. The reattachment length varied with different rotation numbers. Increasing rotation led to a decrease (or increase) in the reattachment length on the unstable (stable) side because the Coriolis force increases (decreases) turbulent mixing near the unstable (stable) side. The enhanced mixing on the unstable side resulted in higher levels of Nusselt number as can be seen in Fig. 9.

Overall, the Nusselt number increases rapidly and reaches a local maximum near the upstream corner of the rib where high levels of turbulent intensities are observed. Then, the Nusselt number decreases near the top of the rib. The Nusselt number keeps decreasing along the rear face of the rib due to the recirculation and increases to the second local maximum near reattachment. The heat transfer on the top of the rib increases about 35% compared to stationary (non-rotating) case near the unstable side, but decreases about 20% near the stable side. Similar order of magnitude differences compared to the stationary case are noticed in the downstream region. The flow pattern of streamlines for Case I (no rotation) and Case III (high rotation) are shown in Fig. 10. The separation bubbles on the front and rear faces of the ribs are clearly visible. Due to the large increasing pressure gradient on the top of the ribs,

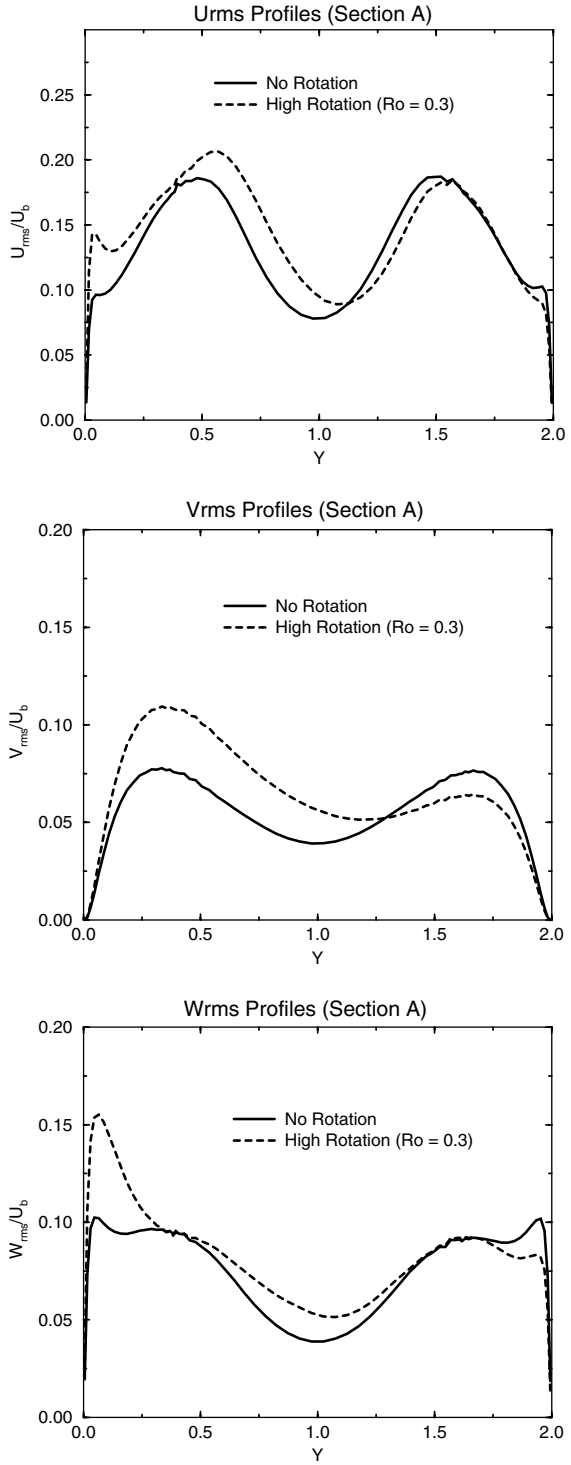

Fig. 8. U_{rms}, V_{rms}, and W_{rms} profiles at section A.

a small separation is induced (see Fig. 9). Behind the ribs, a rapid rise of the static pressure causes a larger

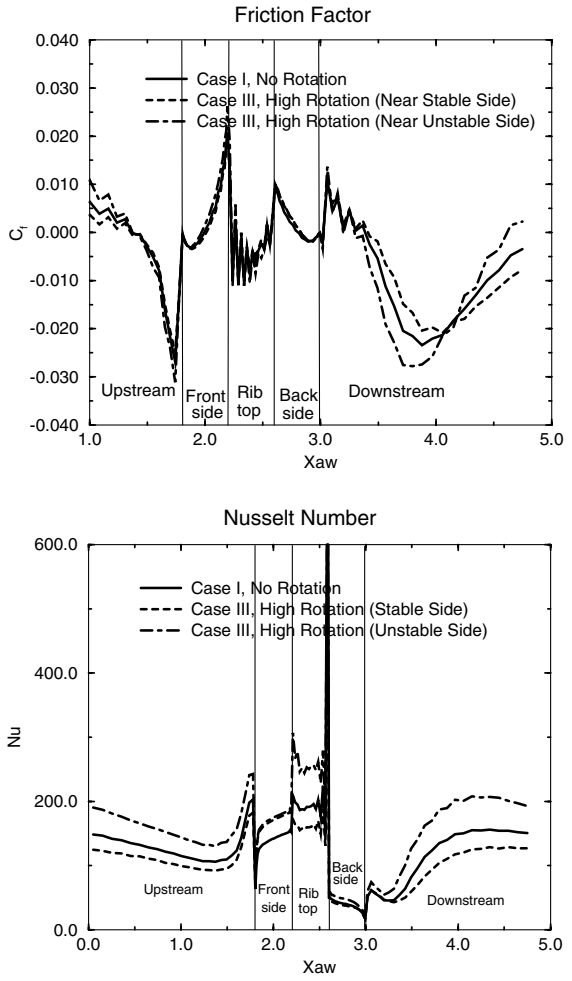

Fig. 9. C_f and Nu profiles at sections B and C (see Fig. 7 for sections B and C).

separation region. For Case I, the reattachment length of the separation region is about 5h (5×rib height) for both walls, but it is about 3h near the unstable side and 5.5h near the stable side for Case III.

6. Conclusions

The LES results (mean velocity and velocity fluctuations) agree well with Piomelli's [3] DNS data for the incompressible isothermal rotating channel flow at a rotation number of 0.144.

Turbulent channel flow with low heating was calculated. Additionally, turbulent channel flows with constant wall heating or cooling rates of magnitudes large enough to cause significant variation in the temperature-dependent fluid properties were simulated. All those

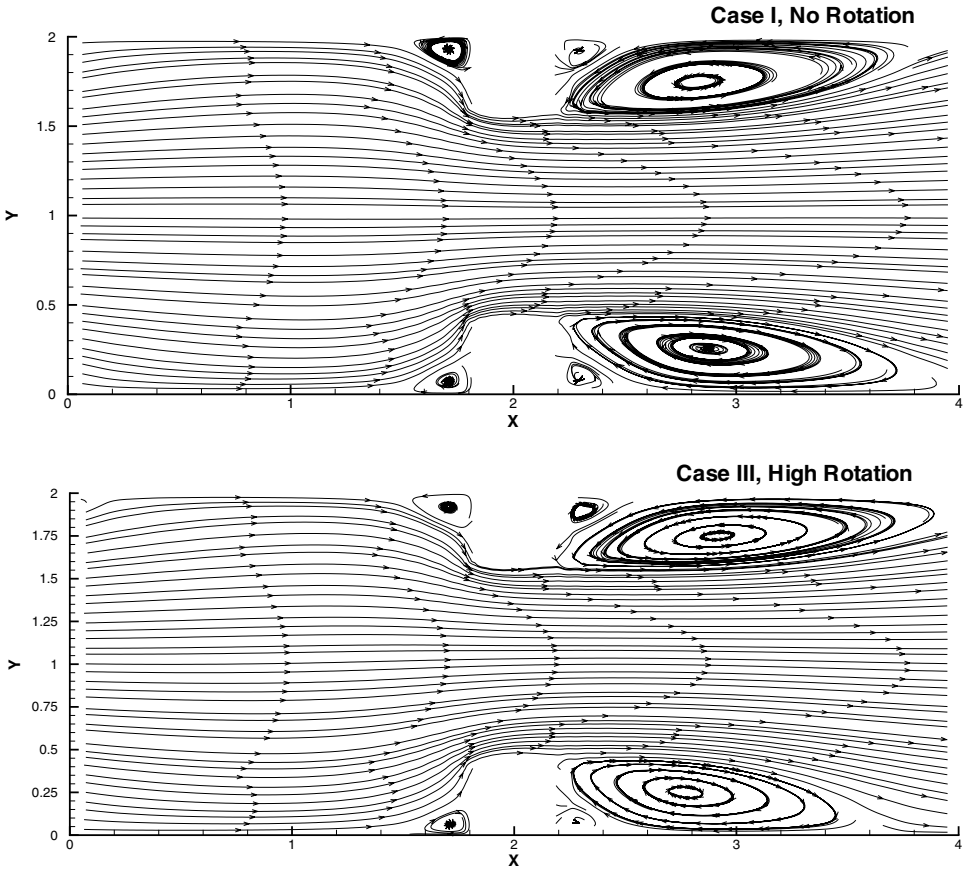

Fig. 10. Streamlines for Cases I and III.

simulations were performed under the influence of spanwise system rotation.

In general, the system rotation was found to suppress turbulent velocity fluctuations and shear stress near the stable side of the channel, but enhance those fluctuations and shear stress near the unstable side. Accordingly, turbulent temperature fluctuations and turbulent heat flux are decreased near the stable side of the channel, but increased near the unstable side of the channel. The streamwise and spanwise rms velocity fluctuations can be seen to differ by about a factor of two near the two walls. The ratio of wall shear stress and heat flux on the two sides ranged between a factor of 2 and 3. The ratio of Nusselt numbers at the two walls was very nearly a factor of 3 as can be seen from Table 1.

The coarse grid DNS gave nearly as good results as LES, except that it overestimated the velocity fluctuations near the wall due to its lack of a dissipation mechanism. In addition, using semi-local coordinates instead of wall coordinates tends to collapse curves of high heating and low heating into that of low heating. It is interesting, too, that the distribution of rms of V velocity is changed significantly (from a two-peak profile to a one-peak profile) due to the Coriolis force acting in the y direction.

An investigation was also conducted on the effects of rotation on the heat transfer in a ribbed channel flow using large eddy simulation. Very consistent results were obtained indicating that rotation stabilizes the leading side and unstabilizes the trailing side. U_{rms}, V_{rms}, W_{rms}, and friction factor, all consistently show that the turbulence structure is greatly altered by the rotation. The turbulence intensity is significantly higher near the unstable side. The reattachment length also shows sensitivity to rotation. The reattachment length on the stable side is increased due to the laminarization, while it is decreased on the unstable side. Rotation also influences the heat transfer in the flow. With rotation, the heat transfer was greatly enhanced on the unstable side and reduced on the stable side. It is found that the temperature profile is no longer symmetric due to the Coriolis force.

Acknowledgements

The current research was partially supported by the Air Force Office of Scientific Research under grants F49620-94-1-0168, F49620-01-1-0113, and F49620-00-1-0229 and by the National Science Foundation under grants CTS-9414052 and CTS-9806989. The computer resources provided by University of Minnesota Supercomputing Institute are gratefully acknowledged.

References

[1] D.J. Tritton, Experiments on turbulence in geophysical fluid dynamics, Turbulence Predict. Geophys. Fluid Dynam. Climate Dynam. (1985) 172–192.
[2] E.J. Hopfinger, Turbulence and vortices in rotating fluids, Theoret. Appl. Mech. (1989) 117–138.
[3] U. Piomelli, J.H. Liu, Large-eddy simulation of rotating channel flows using a localized dynamic model, Phys. Fluids 7 (1995) 839–848.
[4] P. Moin, K. Squires, W. Cabot, S. Lee, A dynamic subgrid-scale model for compressible turbulence and scalar transport, Phys. Fluids A 3 (1991) 2746–2757.
[5] L.D. Dailey, N. Meng, R.H. Pletcher, Large eddy simulation of constant heat flux turbulent channel flow with property variations: quasi-developed model and mean flow results, J. Heat Transfer 125 (2003) 27–38.
[6] J.P. Johnston, H.M. Halleen, D.K. Lezius, Effects of spanwise rotation on the structure of two-dimensional fully developed turbulent channel flow, J. Fluid Mech. 56 (1972) 533.
[7] J.C. Han, Y.M. Zhang, C.P. Lee, Influence of surface heating condition on local heat transfer in a rotating square channel with smooth walls and radial outward flow, J. Turbomach. 116 (1994) 149–158.
[8] R. Kristoffersen, I.H. Andersson, Direct simulations of low-Reynolds-number turbulent flow in rotating channel, J. Fluid Mech. 256 (1993) 163–197.
[9] M. Matsubara, P.H. Alfreson, Experimental study of heat and momentum transfer in rotating channel flow, Phys. Fluids 8 (1996) 2964–2973.
[10] J.C. Han, L.R. Glicksman, W.M. Rohsenow, An investigation of heat transfer and friction for rib-roughened surfaces, Int. J. Heat Mass Transfer 21 (1978) 1143–1155.
[11] G. Bergeles, N. Athanassiadis, The flow past a surface-mounted obstacle, J. Fluids Engng. 105 (1983) 461–463.
[12] E.M. Sparrow, W.Q. Tao, Enhanced heat transfer in a flat rectangular duct with streamwise-periodic disturbances at one principal wall, Trans. ASME J. Heat Transfer 105 (1983) 851–861.
[13] L.E. Drain, S. Martin, Two-component velocity measurements of turbulent flow in a ribbed-Wall flow channel, in: Int. Conf. on Laser Anenometry-Advances and Application Manchester, UK, 1985, pp. 99–112.
[14] J.H. Wagner, B.V. Johnson, R.A. Graziani, F.C. Yeh, Heat transfer in rotating serpentine passages with trips normal to the flow, J. Turbomach. 114 (1992) 847–857.
[15] B. Vreman, B. Geurts, H. Kuerten, Subgrid-modeling in les of compressible flow, Appl. Sci. Res. 54 (1995) 191–203.
[16] L.D. Dailey, R.H. Pletcher, Evaluation of multigrid acceleration for preconditioned time-accurate Navier–Stokes algorithms, Comput. Fluids 25 (1996) 791–811.
[17] M. Germano, Turbulence: the filtering approach, J. Fluid Mech. 238 (1992) 325–336.
[18] W.P. Wang, Coupled compressible and incompressible finite volume formulations for the large eddy simulation of turbulent flow with and without heat transfer, Ph.D. Thesis, Iowa State University, Ames, IA, 1995.
[19] D.K. Lilly, A proposed modification of the Germano subgrid-scale closure method, Phys. Fluids 4 (1992) 633–635.
[20] P.G. Huang, G.N. Coleman, P. Bradshaw, Compressible turbulent channel flow—a close look using DNS data, AIAA paper, 95-0584, 1995.